Mixing in lock-release gravity currents propagating up a slope

L. Ottolenghi,[1] C. Adduce,[1,a)] R. Inghilesi,[2] F. Roman,[3] and V. Armenio[4]

[1]*Department of Engineering, University Roma Tre, Rome 00146, Italy*
[2]*Institute for Environmental Protection and Research, Rome 00144, Italy*
[3]*Iefluids, Piazzale Europa 1, 34127 Trieste, Italy*
[4]*Department of Engineering and Architecture, University of Trieste, Trieste 34127, Italy*

Lock-exchange gravity currents propagating up a slope are investigated by large eddy simulations, focusing on the entrainment and mixing processes occurring between the dense current and the ambient fluid. Relevant parameters, such as the aspect ratio of the initial volume of dense fluid in the lock R, the angle between the bottom boundary and the horizontal direction θ and the depth aspect ratio ϕ, are varied. The numerical results are compared with laboratory experiments and a good agreement is found. Entrainment and mixing in a lock-release gravity current are studied using different entrainment parameters and an energy budget method. The entrainment is found to depend on both Froude, Fr, and Reynolds, Re, numbers. In addition, the dependence of both entrainment and mixing on the parameters varied is discussed. The entrainment decreases with increasing steepness of the bottom and R. Irreversible mixing is not affected by the varied parameters during the slumping phase, while during the successive phases of motion, it is found to decrease with the increase of θ and R. Low entrainment and mixing occur for $\phi < 1$.

I. INTRODUCTION

Gravity currents are buoyancy driven flows in which the density gradient causes the development of the flow predominantly in the horizontal direction. The density difference between the current and the surrounding fluid can be due to temperature or salinity gradients, or due to the presence of suspended particulates. In the latter case, the flow is more properly referred to as a turbidity current. This kind of process widely occurs in the environment, both due to natural or anthropogenic causes. Examples of gravity currents[1] are oceanic overflows, avalanches, sea breeze fronts, sand storms, oil spillages, the spread of a dense gas in the atmosphere and pollutant discharges in water bodies.

Laboratory experiments and numerical simulations have been used to investigate the dynamics of gravity currents. In the laboratory, steady[2,3] and unsteady[4–6] gravity currents are reproduced by releasing a constant discharge or a fixed volume of a dense fluid into a lighter one, respectively. The lock-exchange technique is a simple and useful method to generate unsteady gravity currents. In the lock-exchange experiments, a tank divided in two volumes by a sliding gate is filled with two fluids of different densities. When the gate is removed, a gravity current develops: the dense fluid starts to flow along the bottom of the tank under the ambient fluid and the horizontal pressure gradient drives the motion. The two layers start to mix and different flow regimes can be observed.[7] According to the shallow-water theory for horizontally propagating gravity currents, three phases can be developed: a first *slumping* phase characterized by a constant front velocity; a second *self-similar* phase during which the current slows down; and a third *viscous* phase if viscous forces become important.

a)Electronic mail: claudia.adduce@uniroma3.it

While lock-release gravity currents flowing over horizontal and down-sloping bottoms have been widely studied in the literature,[8–11] to the best of our knowledge, few studies on gravity currents flowing up a slope have been carried out.[12–14] This latter case is not rare in nature and deserves investigation. Sea breeze fronts flowing over irregular coastal inlands, oceanic flows propagating over a complex bathymetry, and the nocturnal-valley breeze are examples of gravity currents propagating up the sloping boundaries. Marleau, Flynn, and Sutherland[12] carried out laboratory experiments on lock-release gravity currents flowing up a slope and developing the slumping phase only. Their experiments were configured to lead the current to flow first along a horizontal bed and then to climb up a sloping bottom. They found the deceleration to be dependent on the reduced gravity driving the motion, the inclination of the slope, and the ratio between the initial depths of the dense and the ambient fluids. Laboratory experiments as well as shallow water simulations of lock-release, up-sloping gravity currents were performed by Lombardi et al.[13] They found that during the slumping phase the upslope does not affect the velocity of the front propagation, while for later times the steeper the bottom upslope, the higher the deceleration of the current. Finally, laboratory experiments and hydrostatic numerical simulations were carried out by Jones et al.[14] to analyse the front velocity of gravity currents in a rectangular channel and V-shaped valley propagating both horizontally and up a small slope. The literature survey shows that although a few recent studies have investigated the effect of an upslope on a gravity current's front propagation, there remains a lack of knowledge on how an upslope affects entrainment and mixing in lock-release gravity currents.

The evaluation of mixing occurring between a dense current and the ambient fluid is an important issue since it affects the buoyancy forces driving the motion. The entrainment of ambient fluid in gravity currents flowing over horizontal or downsloping boundaries was investigated in both laboratory experiments and field measurements. In Cenedese and Adduce[3,15] the entrainment in a steady gravity current flowing downslope was investigated and the dependency of the entrainment parameter on both Froude and Reynolds numbers was highlighted. The entrainment in a lock-release, horizontally propagating gravity current flowing over a smooth and a rough bottom was recently studied in Adduce, Sciortino, and Proietti[9] and in Nogueira et al.,[16,17] respectively.

The dynamics of gravity currents have been widely studied by means of simplified shallow water models, which are often based on the assumption of mass conservation and thus entrainment effects are not always considered. Recent investigations introduced the effect of the entrainment in shallow water simulations of lock-release gravity currents[9,13,18] and found that the entrainment of ambient fluid affects the numerical results. In particular, in the investigations of Ross, Dalziel, and Linden[18] and Adduce, Sciortino, and Proietti,[9] two-layer shallow water simulations with and without entrainment were compared to laboratory experiments, showing a better agreement when mixing was accounted for. Nevertheless, there is still a lack of knowledge on the suitable entrainment parametrization to be used in the framework of simplified two-layer shallow water models. Therefore, information on entrainment and mixing provided by three-dimensional highly resolved numerical simulations can be used to improve two-layer shallow water models simulating lock-release gravity currents.

The application of high-resolution numerical models to solve the Navier-Stokes equations in the investigation of gravity currents dynamics is relatively recent. Direct Numerical Simulation (DNS) and the computationally less expensive Large Eddy Simulations (LESs) have been used for this purpose.[19–22] Several investigations have been carried out with DNS and LES to study gravity currents in different configurations.[11,23–25] A first attempt to study the effect of an up-sloping bottom on the development of a gravity current by LES is given by Safrai and Tkachenko.[26] In this work, two cases with an up-sloping angle were presented ($\theta = 5°$, $\theta = 10°$), showing a less energetic three-dimensional turbulent pattern of the gravity current flowing along the up-sloping bottom, compared to the down-sloping cases.

The aim of the present paper is to investigate entrainment and mixing in unsteady gravity currents flowing up mild slopes using LES. The purpose is to reproduce the dynamics of geophysical flows propagating in a deep non-bounded ambient fluid driven by buoyancy forces on complex boundaries. Our aim is to address the following main research questions:

1. How are the current dynamics affected by the presence of an upsloping boundary?
2. What is the effect of relevant dimensionless parameters, such as the bottom upslope, the aspect ratio of the initial volume of the gravity current, and the depth aspect ratio, on both entrainment and mixing in a lock-release gravity current?
3. How do the present entrainment evaluations in lock-release gravity currents flowing up a slope compare with previous findings on gravity currents flowing over flat and downsloping bottoms?

To address the questions above, we systematically perform three-dimensional large eddy simulations with different upslope angles ($\theta = 0°$, $\theta = 1.4°$, $\theta = 2.5°$, and $\theta = 5°$), and different aspect ratios of the initial volume of the gravity current ($R = 2$, $R = 1$, and $R = 0.67$). In addition, two simulations are performed varying the depth ratio ϕ in order to study partial-depth gravity currents flowing up a slope. Laboratory experiments with $\theta = 0°$ and $\theta = 1.4°$ are also performed, and comparisons with the numerical data are carried out in order to assess the reliability of the model implementation. The effects related to the presence of a sloping boundary on the main dynamics of a gravity current are investigated through the analysis of the numerical density fields. Then, different entrainment parameters are defined and evaluated, and comparisons with the entrainment in steady gravity currents flowing downslope are presented. Finally, mixing is evaluated through the application of the energy budget method of Winters et al.[27]

The present paper is organized as follows. In Sec. II the problem formulation is presented and the numerical model is described; in Sec. III a comparison between laboratory experiments and numerical results is given and the main effects of the inclined bottom on the flow dynamics are highlighted. Evaluation of the entrainment is presented in Sec. IV and the potential energy budget is shown in Sec. V. Finally, conclusions are given in Sec. VI.

II. PROBLEM FORMULATION AND NUMERICAL MODEL

Figure 1 shows a sketch of the configuration for the simulations of lock-release gravity currents flowing up a slope. A fluid of density ρ_1 fills a volume with a lock length x_0, while a light ambient fluid of density ρ_0 (with $\rho_0 < \rho_1$) fills the rest of the tank. The depths of the ambient fluid and the dense fluid in the lock are referred to as H and h_0, respectively, with $H = 0.2$ m. θ is the angle between the bottom of the tank and the horizontal direction and $s = \tan\theta$ is the inclination of the bottom boundary. The aspect ratio $R = h_0/x_0$ is varied by changing x_0 and three different configurations of the initial lock volume are tested: $R = 2$, $R = 1$, and $R = 0.67$. Most of the numerical simulations are run with $\phi = h_0/H = 1$, i.e., full-depth gravity currents, but two cases with $\phi = 0.5$ are also presented. The two fluids are initially separated by a gate and once the gate is removed a gravity current forms: the denser fluid moves rightwards along the bottom of the tank, while the lighter fluid moves leftwards along its top. The fluid densities ρ_1 and ρ_0 are chosen in order to obtain the initial reduced gravity $g_0' = 0.29$ m/s^2, defined as

$$g_0' = g \, \frac{\rho_1 - \rho_0}{\rho_0}. \tag{1}$$

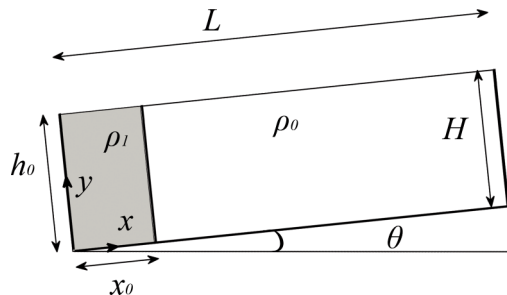The Reynolds number, Re, and the Froude number characterizing the slumping phase, Fr$_{sl}$, are defined as

FIG. 1. Schematic view of the lock-exchange configuration in an upsloping channel.

$$\text{Re} = \frac{u_b H}{\nu}, \tag{2}$$

$$\text{Fr}_{sl} = \frac{U_{sl}}{\sqrt{g'_0 h_0 \cos \theta}}, \tag{3}$$

where ν is the kinematic viscosity, U_{sl} is the velocity during the slumping regime, and u_b is the buoyancy velocity, defined as

$$u_b = \sqrt{g'_0 H}. \tag{4}$$

The simulations with $\phi = 1$ are characterized by $\text{Re} = 48\,522$, while the $\phi = 0.5$ cases are carried out with $\text{Re} = 17\,155$. The numerical parameters are reported in Table I, together with the parameters used in the laboratory experiments, and the latter described in Sec. III.

We use the model of Armenio and Sarkar,[28] which has been widely validated and employed over the years to simulate a large variety of flow fields.[29–31] The numerical model solves the filtered Navier-Stokes equations (the overbar in the following equations $\bar{\Box}$ denotes the LES filtering operation), with a finite difference second-order accurate scheme, under the Boussinesq approximation for buoyancy effects. The governing equations read as

$$\frac{\partial \bar{u}_j}{\partial x_j} = 0, \tag{5}$$

$$\frac{\partial \bar{u}_i}{\partial t} + \frac{\partial \bar{u}_j \bar{u}_i}{\partial x_j} = -\frac{1}{\rho_0}\frac{\partial \bar{p}}{\partial x_i} + \nu \frac{\partial^2 \bar{u}_i}{\partial x_j \partial x_j} - \frac{\rho'}{\rho_0} g \delta_{ij=1,2} - \frac{\partial \tau_{ij}}{\partial x_j}, \tag{6}$$

$$\frac{\partial \bar{s}}{\partial t} + \frac{\partial \bar{u}_j \bar{s}}{\partial x_j} = k_s \frac{\partial^2 \bar{s}}{\partial x_j \partial x_j} - \frac{\partial \lambda_j}{\partial x_j}, \tag{7}$$

where u_i denotes the velocity component in the x_i direction of the computational domain (also referred to as x, y, and z), corresponding to the streamwise, the bottom wall-normal, and the spanwise directions, respectively. The terms p and s in (6) and (7) are the hydrodynamic pressure and the salinity, respectively. ρ' is the variation of density with respect to the reference value ρ_0 (corresponding to the reference salinity s_0). The density variation is due to the salinity concentration gradients only, since the temperature is kept constant. Thus, the state equation reads as

$$\rho = \rho_0 \left[1 + \beta(s - s_0) \right], \tag{8}$$

where β is the salinity contraction coefficient. ν and k_s in (6) and (7) are the kinematic viscosity and the molecular salt diffusivity, respectively. The effect of the sloping bottom on the dynamics

TABLE I. Parameters of LES and laboratory experiments.

Name	θ (deg)	R	ϕ	Re	Fr_{sl}
RUN0	0.0	2	1	48 522	0.43
RUN1	1.4	2	1	48 522	0.42
RUN2	2.5	2	1	48 522	0.42
RUN3	5.0	2	1	48 522	0.40
RUN4	1.4	1	1	48 522	0.42
RUN5	2.5	1	1	48 522	0.41
RUN6	1.4	0.67	1	48 522	0.42
RUN7	2.5	0.67	1	48 522	0.40
RUN8	1.4	1	0.5	17 155	0.47
RUN9	2.5	1	0.5	17 155	0.47
EXP0	0.0	2	1	48 345	0.40
EXP1	1.4	2	1	48 508	0.37
EXP2	1.4	1	1	48 467	0.43
EXP3	1.4	0.67	1	48 385	0.42

of a gravity current is reproduced in the numerical model considering the components of the gravitational acceleration g:[10,11] the first component is oriented orthogonally to the bottom, and the second component of g is oriented along the x-axis, in the upstream direction. Thus, g acts on the first and second components δ_{ij} (9) of the momentum equation (streamwise and bottom wall-normal directions),

$$
\delta_{ij} = \begin{cases} \sin\theta & \text{if } i = j = 1 \quad \rightarrow x-\text{direction} \\ \cos\theta & \text{if } i = j = 2 \quad \rightarrow y-\text{direction} \\ 0 & \text{if } i = j = 3 \quad \rightarrow z-\text{direction} \\ 0 & \text{if } i \neq j \end{cases} \tag{9}
$$

The LES methodology consists of the separation of the large scales of motion that are directly solved, through a three-dimensional unsteady numerical integration of the governing equations, and the small and dissipative scales of turbulence, which are modelled as subgrid stresses (SGSs).[32] The SGS momentum and salinity fluxes τ_{ij} and λ_j in Equations (6) and (7) are modelled using the dynamic Smagorinsky eddy viscosity model. Further details about the numerical model can be found in Armenio and Sarkar.[28] The Lagrangian approach of Meneveau, Lund, and Cabot[33] is used to calculate the constants of the model, needed for the estimation of the SGS viscosity and diffusivity ν_t and k_t. Note that in the present model, ν_t and k_t are calculated independently according to the dynamic methodology, and hence, the SGS Schmidt number, not set *a priori*, is a result of the simulation. This is a noteworthy feature of the model, particularly when transitional flows such as the present one are simulated. The semi-implicit fractional-step method of Zang, Street, and Koseff[34] is applied to integrate the governing equations. The time advancement of the convective terms is calculated through the second-order Adams-Bashforth technique. The algorithm resolves the diagonal diffusive terms through the implicit Crank-Nicolson scheme, while a second-order centered scheme discretizes the spatial derivatives. Finally, the pressure equation is solved with a multigrid-SOR algorithm.

In order to compare numerical simulations with the laboratory experiments, the physical parameters are consistent with those used in the experiments. Specifically, the dimensions of the numerical domain in the bottom wall-normal and in the spanwise directions are $L_y = L_z = 0.2$ m. For computational reasons, the length of the domain in the streamwise direction is 4.096 m, corresponding to $20.48H$ (comparisons with laboratory experiments and data analysis are made only for the first 3 m). Flat, no-slip surfaces are set as boundary conditions in the streamwise direction and at the bottom of the tank ($x = 0$, $x = L_x$ and $y = 0$). A shear-free boundary condition is applied at the top boundary ($y = H$) as suggested by Liu and Jiang[35] and periodicity conditions are employed in the spanwise direction instead of the real rigid surfaces present in the laboratory. This allows us to focus on the effects of the up-sloping bottom without dealing with three-dimensional effects arising from the presence of the lateral walls, and thus to investigate the dynamics of gravity currents of large relative width. The computational grid is composed of $2048 \times 128 \times 64$ cells, respectively, in the streamwise, bottom wall-normal, and spanwise directions. The grid spacing is defined as follows: $\Delta x = 0.01H$; $\Delta z = 0.016H$; Δy ranges from $0.01H$ at the top to $0.002H$ at the bottom of the domain. These spacings are quite similar to the ones used in Tokyay, Constantinescu, and Meiburg[24] in which LESs of gravity currents, characterized by Re of the same order of magnitude as our cases, were performed. In particular, the *a posteriori* analysis of the velocity field ensured that the grid spacing used is sufficient to resolve the viscous sublayer, avoiding the use of wall layer models. Specifically, it was verified that the dimensionless grid size was $\Delta x^+ < 50$, $\Delta z^+ < 20$, and $\Delta y^+_{wall} \sim 1$ at the bottom surface. The grid spacing is made non-dimensional with u_τ/ν, where $u_\tau = \sqrt{\tau_w/\rho}$ is calculated using the time dependent maximum wall shear stress during the evolution of the gravity current.

A constant value of the Courant number equal to 0.6 is adopted for all simulations. The Schmidt number Sc, defined as the ratio between the kinematic viscosity and the molecular diffusivity, is fixed at the salt water reference value Sc = 600.

At $t = 0$ a spatial distribution of the scalar with a discontinuity located at $x = x_0$ is prescribed, with an initial density value $\rho = \rho_1$ for $x < x_0$ and $\rho = \rho_0$ for $x \geq x_0$. Zero flux of the scalar is

imposed at the boundaries. The flow field is initialized with the fluid at rest everywhere. Ten different simulations, denoted hereafter RUN0-RUN9, were performed, varying the inclination of the bed θ, the initial aspect ratio of the lock volume R, and the depth ratio ϕ.

III. NUMERICAL RESULTS AND COMPARISON WITH LABORATORY EXPERIMENTS

Laboratory experiments were performed at the Hydraulics Laboratory of the University *Roma Tre*. A Plexiglas tank 3 m long, 0.2 m wide, and 0.3 m deep was used to perform the lock-exchange experiments, similar to the one described in Nogueira *et al.*[16,36] The tank is divided into two different volumes by a removable gate, placed at a distance x_0 from the left wall of the tank. Salty water of density ρ_1 fills the volume on the left hand side of the gate, while fresh tap water is used to fill the rest of the tank (with a measured density $\rho_0 < \rho_1$). A controlled quantity of dye (E171, titanium dioxide) is added to the salty water in order to assure the visibility of the dense fluid. A pycnometer is used to measure the density. The tank can be inclined at different angles θ in order to perform experiments of gravity currents propagating up the mild slopes. The flow generated in the laboratory experiments is a lock-release full-depth gravity current and the aspect ratio R is varied.

The experiment starts with the removal of the gate, when the column of fluid in the lock collapses and starts to move along the bottom of the tank. A gravity current is thus generated, and it develops under the lighter (ambient) fluid. As the gravity current propagates downstream, the light fluid flows upstream by continuity, and mixing occurs at the interface between the two layers: the dense current entrains ambient fluid and dilutes.[13,17] The experiments are recorded by a CCD camera with an acquisition frequency of 25 Hz and a resolution of 768×576 pixels. The recorded black and white images are first converted to matrices of grey levels with values between 0 (black) and 255 (white), and then they are analysed using a threshold method.[9,13] In this way, the position of the interface between the dense and the light fluids is detected with an accuracy of 4 mm. Four laboratory experiments are performed, testing two different angles $\theta = 0°$ and $\theta = 1.4°$ and three values of R (see Table I). In addition, for two experiments (i.e., EXP0 and EXP1), the spanwise averaged density field was measured using the technique described in Nogueira *et al.*[16]

In order to analyse the numerical data, a dimensionless density field, ρ^*, is defined as

$$\rho^*(x, y, z, t) = \frac{\rho(x, y, z, t) - \rho_0}{\rho_1 - \rho_0}. \tag{10}$$

The gravity current studied in the present experiments is essentially two-dimensional, with three-dimensional effects developing in the cross-sectional plane being negligible compared to the main two-dimensional features. To detect the main features of front position, a side-view of the advancement in time of the current is recorded during each laboratory experiment. In order to make comparisons between three-dimensional LESs and experiments, averaged quantities along the spanwise direction of homogeneity are considered. Hereafter, the averaging operation on the homogeneous z-axis is shown by the symbol $\langle \ \rangle$. In this way, the spanwise averaged density field $\langle \rho^* \rangle$ is analysed, and the iso-density level corresponding to $\langle \rho^* \rangle = 0.02$ is chosen as the interface between the gravity current and the ambient fluid, in agreement with previous laboratory investigations.[16,17,36] In addition, one of the objectives of the present study is to investigate the entrainment in lock-release gravity currents in order to make a contribution to the entrainment parametrization for simplified models which are not able to resolve the small scale mixing processes. For example, two-layer shallow water models need to parametrize the entrainment by source or sink terms in the continuity equations[9,13,18] and the ambient fluid is assumed to not vary its density. Consequently, in the present study, the iso-density level $\langle \rho^* \rangle = 0.02$ is chosen to define the interface between the two fluids in order to be consistent with the shallow water model formulations and, hence, considering the dense current as the portion of the fluid that is not purely ambient fluid.

The front position x_f is defined as the streamwise coordinate of the nose of the dense current, at a distance of 4 mm from the bed. This definition is the same as in the laboratory experiments. The numerical and experimental values of x_f versus time are plotted in Figure 2(a), showing a good agreement for all the cases considered. Figure 2(b) shows $x_f(t)$ for all the numerical simulations performed. In Figures 2(a) and 2(b), the greater θ, the more bent the curve of $x_f(t)$, because
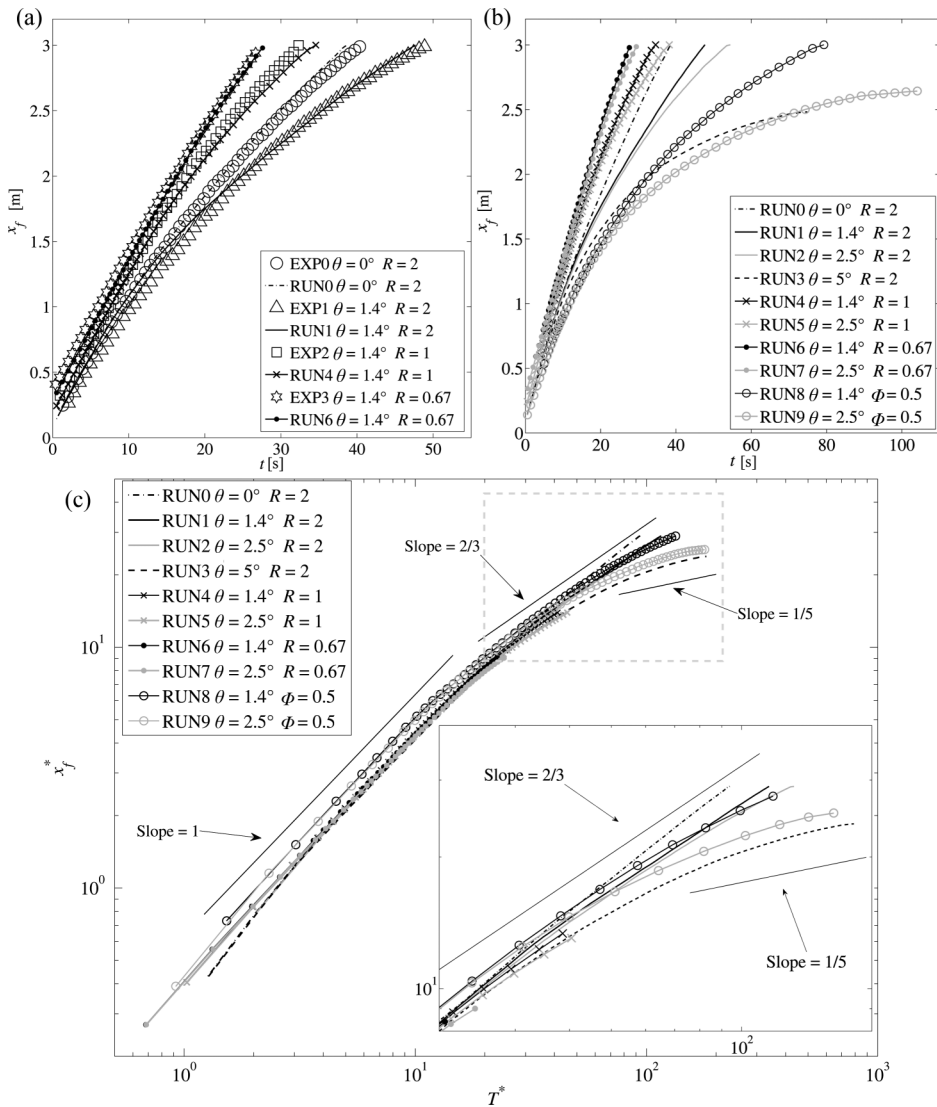
FIG. 2. (a) Front position versus time: comparison between numerical simulations and laboratory experiments; (b) numerical front position versus time; (c) dimensionless numerical front position versus time in log-log scale.

the gravity current slows down more abruptly. The effect of the inclination of the bottom on the dynamics of a dense current with $R = 2$ becomes evident after a distance of about 9 lock-lengths ($x_f > 0.9$ m), when curves relative to different runs start to diverge. In RUN3 ($R = 2$ and $\theta = 5°$), the steep inclination of the bottom prevents the density current from reaching the end-wall of the tank and it stops at $x = 2.5$ m. A similar behaviour is observed in RUN9 ($R = 1$, $\phi = 0.5$ and $\theta = 2.5°$). In fact, the partial-depth cases slow down more effectively than the $\phi = 1$ cases, due to the smaller volume of dense fluid released at the beginning of the simulation. However, in all of the cases considered, at fixed values of R and ϕ, the velocity of the gravity current decreases as θ increases.

In order to study the phases of development of the gravity currents,[1] the dimensionless front position x_f^* and the dimensionless time T^* are defined as

$$x_f^* = \frac{x_f(t) - x_0}{x_0},$$ (11)

$$T^* = \frac{t \, u_b}{x_0}.$$ (12)

A log-log plot of x_f^* versus T^* is shown in Figure 2(c) for all simulations. The propagation of a gravity current over a horizontal bed, according to the shallow-water theory, is commonly divided into different phases of spreading,[7] namely a slumping phase, a self-similar phase, and a final viscous phase. The up-sloping cases are analysed here using the same scaling laws commonly adopted for the horizontal configurations. During the slumping phase, the gravity current is characterized by a constant front velocity. The slumping phase is clearly visible in all of the simulations of Figure 2(c) (solid line with slope = 1). No differences are detected among the cases analysed in Figure 2(c) during the constant velocity regime, indicating that a gentle upslope does not significantly affect the slumping phase of lock-release gravity currents. Thus, a good agreement between the present gravity currents flowing over mild upslopes and the shallow water theory developed for gravity currents propagating over horizontal boundaries is found during the slumping phase. During the self-similar phase, the current slows down and x_f^* follows the theoretical power law $t^{2/3}$, as shown in Figure 2(c) by the thin solid line with slope = 2/3. Later, the front velocity decreases faster, viscous forces influence the motion, and the slope of x_f^* continuously decreases (until the current finally stops for RUN3 and RUN9). In Figure 2(c), the thin solid line with slope = 1/5 marks the viscous phase commonly referred to in gravity currents flowing over horizontal boundaries. A zoom of these subsequent phases is shown in Figure 2(c) in order to better detect the differences among the runs. Depending on R and θ, different flow regimes are observed. Nevertheless, a deceleration of the current is visible for all of the simulations after $x_f^* \sim 9$. In the $R = 2$ cases and in the partial-depth cases, the influence of θ during the self-similar regime is clearly visible. Moreover, at the end of RUN3 and RUN9, the currents strongly decelerate, viscous forces influence the motion, and a viscous phase occurs. Thus, during the slumping phase, small differences are found among the upsloping cases analysed herein and the run propagating along a horizontal bottom, as in the laboratory experiments of Lombardi et al.[13] This behaviour is not in agreement with the results of Marleau, Flynn, and Sutherland,[12] who found a significant deceleration of the gravity current during the slumping phase. These different findings are probably due to the different geometries of the experimental setups and to the different slopes tested, which are here much smaller than the ones considered in Marleau, Flynn, and Sutherland[12] (values of slopes ranging from 0.25 and 1.13, corresponding to angles between 14° and 48.5°). On the other hand, a good agreement is found with Lombardi et al.,[13] which used a range of angles similar to the ones considered herein (0°−1.8°, without variations of R and ϕ).

The post-processing of the LES data yields highly resolved spanwise-averaged density fields of the simulated gravity currents for all runs. In order to investigate the effect of an upslope on the propagation of the gravity current, $\langle \rho^* \rangle$ at $T^* \cong 85$ is shown in Figure 3 for a fixed $R = 2$ and different values of θ (RUN0-RUN3). As expected, as the upslope increases the gravity current slows down, the thickness of the gravity current becomes smaller and smaller, and the interface between the dense and the ambient fluids appears smoother (Figures 3(a) and 3(d)). This is all in agreement with the reduced turbulence observed by Safrai and Tkachenko.[26] In the upsloping cases, as the dense current propagates part of the fluid in the tail region detaches from the rest of the current and starts to flow backwards. In fact, while the head of the current flows in the positive x-axis direction, part of the tail propagates to the left wall of the tank, where an accumulation region develops, in agreement with Lombardi et al.[13] and Marleau, Flynn, and Sutherland.[12] For this reason, high values of density are found at the beginning of the tank, and the tail region can be thicker than the head. The backward flow is more pronounced at higher θ. For example, in RUN3, after $T^* = 85$, most of the dense fluid flows backward and stratifies at the beginning of the tank; only a thin gravity current continues to climb up the slope, becoming thinner and thinner until it completely stops, before reaching the right wall of the tank (Figure 3(d)).

The inevitable small differences that are observed between the numerical results and the laboratory experiments are mainly associated with the effects of the gate removal, which is far from the numerical ideal operation. Small influences are also related to the boundary conditions imposed in the model, which are similar, but not equal, to the experimental conditions, especially the one imposed at the top boundary. Nevertheless, from the analysis of the front positions (Figure 2(a)), it is possible to say that a good level of agreement between laboratory experiments and numerical simulations is found. In addition, as it will be discussed in Sec. IV, also the quantitative comparison
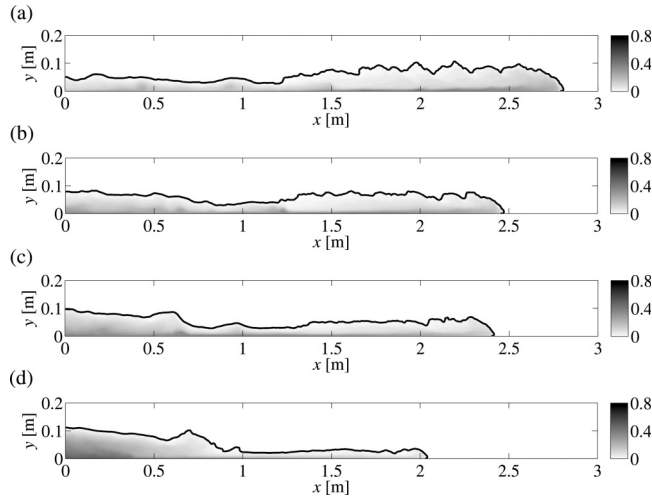
FIG. 3. Dimensionless density fields for different numerical simulations ($R = 2$ cases) at $T^* \cong 85$: (a) RUN0 ($\theta = 0°$); (b) RUN1 ($\theta = 1.4°$); (c) RUN2 ($\theta = 2.5°$); (d) RUN3 ($\theta = 5°$).

between the numerical and the laboratory entrainment parameters shows a good agreement. This confirms that the present LESs are not only able to capture the front propagation of the gravity current, but the increase of the current volume, due to the entrained ambient fluid, is well predicted, too.

IV. ENTRAINMENT PARAMETER

When a gravity current propagates, it entrains ambient fluid, increasing in volume. This process can be parametrized using a dimensionless entrainment velocity as described in Cenedese and Adduce:[3] the entrainment velocity is evaluated as the flow of ambient fluid crossing the interface between the dense current and the light fluid, per unit area. In this context, a bulk entrainment flow Q_{ei} and a local entrainment flow Q_{ei_local} are here defined as

$$Q_{ei} = \frac{(A_i - A_0)d}{t_i - t_0}, \tag{13}$$

$$Q_{ei\_local} = \frac{(A_i - A_{i-1})d}{t_i - t_{i-1}}, \tag{14}$$

where t_i is a certain time, t_0 is the initial time $t = 0$, and t_{i-1} is the former time of t_i. A_i and A_{i-1} are the areas under the iso-density level $\langle \rho^* \rangle = 0.02$ in the x-y plane at t_i and t_{i-1}, respectively. A_0 is the initial area of the dense current at t_0 and d is the width of the tank. The bulk entrainment velocity, W_{ei}, and the local entrainment velocity, W_{lei}, are defined as

$$W_{ei} = \frac{Q_{ei}}{S_i}, \tag{15}$$

$$W_{lei} = \frac{Q_{ei\_local}}{\frac{1}{2}(S_i + S_{i-1})}, \tag{16}$$

where the surfaces S_i and S_{i-1} are the interfaces separating the gravity current and the ambient fluid at t_i and t_{i-1}. Due to the complexity of the form of the real interface dividing the dense and the ambient fluids, it is approximated here by the product $(x_{f\_i} \cdot d)$ at each t_i.

The entrainment parameter is a dimensionless entrainment velocity. In this work, the difference between the bulk velocity of the dense current and the bulk velocity of the ambient fluid is used as a velocity scale.[13,17,37] The bulk and the local entrainment parameters, E_{bulk} and E_{local}, can be defined as

$$E_{bulk} = \frac{W_{ei}}{2\,U_i}, \tag{17}$$

9

$$E_{local} = \frac{W_{lei}}{(U_i + U_{i-1})}, \qquad (18)$$

where U_i and U_{i-1} are the front velocities of the current at times t_i and t_{i-1}, respectively.

The entrainment parameter can be affected by the value of the iso-density threshold used to define the interface between the ambient and the dense fluids.[4] However as discussed in Sec. III, the value of $\langle \rho^* \rangle = 0.02$, used in this study, was selected in order to be consistent with previous studies[3,16,17,36] and with the two-layer shallow water approach. Variations of this threshold in the range of 1%–5% ($0.01 \leq \langle \rho^* \rangle \leq 0.05$) do not significantly affect the present entrainment evaluations. In addition, mixing is also evaluated by an energy method which is not dependent on the iso-density threshold chosen to define the interface, as shown in Sec. V.

The variation of E_{bulk} and E_{local} versus $(x_f - x_0)/H$ is shown in Figure 4 for the cases characterized by $R = 2$, and in Figure 5 for the other cases analysed. E_{bulk} is a decreasing function of x_f^*, indicating that the rate of the entraining volume decreases in time. Even though the behaviour of E_{bulk} is similar in all simulations, small differences are found in the final part of the runs. E_{bulk} at the end of the simulation is related to the total volume of ambient fluid entrained by the gravity current. An increase in θ causes a decrease of the final value of E_{bulk} (Figure 4). The analysis of E_{local} reveals a less smooth behaviour than E_{bulk}. Focusing on the cases with $R = 2$, two main peaks are visible in Figures 4(a)–4(c). These peaks become more complex as the inclination of the tank increases. The second peak is not evident in RUN3 (Figure 4(d)). The presence of local maxima in E_{local} can be related to the modification of the mixing processes during the development of the gravity current. For gravity currents propagating over horizontal boundaries (i.e., RUN0), peaks of E_{local} are related to the trapping of ambient fluid into the body of the dense current due to the development of Kelvin-Helmholtz billows. Qualitatively, similar features are also observed in the gravity currents propagating up a slope. When the billows grow in size and in intensity, light fluid is captured in their structures causing an increase of volume, i.e., fluid-trapping process. In the up-sloping cases, the dense current slows down due to the action of gravity and becomes thinner. The shear stress at the interface between the dense fluid and the ambient one decreases with the decrease of the speed of the dense flow, and the resulting instabilities are less intense. The differences in the conformation of the instabilities make the local entrainment parameter more irregular with the increase of θ.
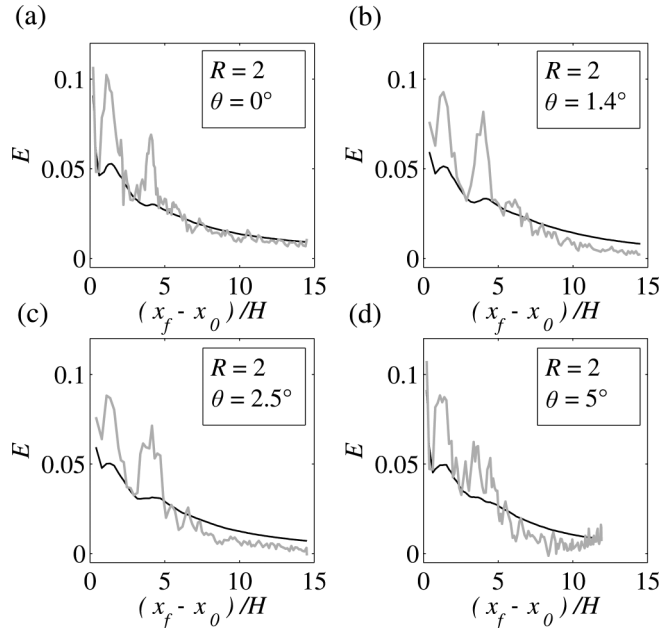

FIG. 4. Bulk entrainment parameter (black line) and local entrainment parameter (grey line) versus the dimensionless front position for $R = 2$ cases: (a) RUN0; (b) RUN1; (c) RUN2; (d) RUN3.
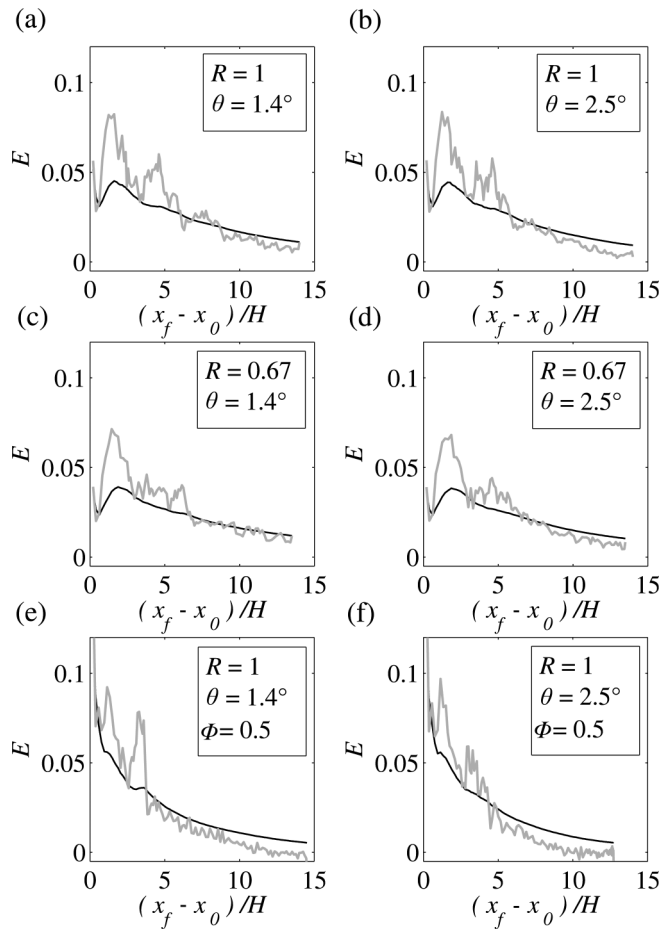
FIG. 5. Bulk entrainment parameter (black line) and local entrainment parameter (grey line) versus the dimensionless front position: (a) RUN4, (b) RUN5, (c) RUN6, (d) RUN7, (e) RUN8, and (f) RUN9.

A similar behaviour is observed in the cases with $R \leq 1$ (Figure 5). The final values of the bulk entrainment parameter, at fixed θ, increase for small values of R. On the other hand, the peaks in E_{local} are less pronounced in the cases with $R = 0.67$ than in the cases with $R = 2$, indicating that the fluid-trapping process described above occurs less frequently. However, the total amount of ambient fluid entrained by the dense current is larger in the $R = 0.67$ cases than in $R = 2$ cases. A similar trend was observed by Ottolenghi et $al.$[31] for gravity currents flowing over a flat bed. A discontinuous behaviour of the local entrainment parameter, characterized by the presence of two peaks, is also visible in the $\phi = 0.5$ cases (Figures 5(e) and 5(f)). For a fixed θ and R, the final value of E_{bulk} is lower in the partial-depth cases (Figures 5(e) and 5(f)) than in the full-depth cases (Figures 5(a) and 5(b)). Furthermore, both E_{bulk} and E_{local} decrease faster in the $\phi = 0.5$ cases than in the $\phi = 1$ cases. Finally, in all of the simulations performed, for a fixed R, both E_{bulk} and E_{local} decrease with the increase of the slope of the bottom θ.

Studies conducted in a wide range of experimental conditions emphasized the dependence of the entrainment parameter on both Reynolds and Froude numbers.[3,15] In addition, the total amount of entrained fluid was observed to also depend on the length of the path followed by the dense current.[3] Figure 6 shows the values of the bulk entrainment parameter at the end of all the simulations versus Reynolds and Froude numbers and the bed's slope. The bulk entrainment parameters evaluated in the laboratory for EXP0 and EXP1 are also reported in the same figure. In RUN3 there are no available values of E_{bulk} for $x_f > 2.5$ m because the dense current stops before reaching the end-wall of the tank. In order to have comparable values of the final bulk entrainment parameter, E_{bulk} is
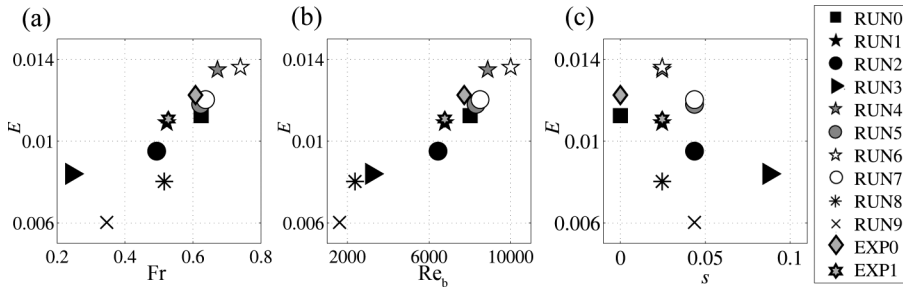
FIG. 6. Numerical and experimental bulk entrainment evaluated after the current has travelled for 2.4 m versus (a) bulk Froude number, (b) bulk Reynolds number, and (c) slope of the bed.

considered after the current flowed 2.4 m in all cases. Bulk Froude, Fr, and Reynolds, Re_b, numbers can be defined, respectively, as

$$Fr = \frac{U}{\sqrt{g'_m \frac{h_0}{2} \cos\theta}}, \tag{19}$$

$$Re_b = \frac{U \, h_0/2}{\nu}, \tag{20}$$

where g'_m is the mean value of the reduced gravity between the initial and the final configuration of the gravity current, and U is a velocity scale defined as the ratio between a length scale L and a time scale T. L is chosen as $L = 2.4$ m and T is the time taken by the gravity current to travel a distance of 2.4 m. E_{bulk} at the end of all the simulations is of the order of magnitude of 10^{-2}, in agreement with Adduce, Sciortino, and Proietti[9] and Nogueira et al.,[17] who investigated the entrainment in lock-release gravity currents. In addition, the entrainment parameters predicted by the LESs for RUN0 and RUN1 are in good agreement with the measured ones. The present numerical simulations are not only able to capture the front propagation (as shown in Sec. III) but also the final amount of the entrained ambient fluid. This latter result gives an additional confirmation of the reliability of the present numerical results. The dependence of E_{bulk} on Re_b and on Fr, in agreement with the previous findings of Cenedese and Adduce[3] and Nogueira et al.,[17] is also verified in the present runs, as shown in Figures 6(a) and 6(b), respectively: E_{bulk} increases as Fr or Re_b increases. In Figure 6(c), the entrainment parameter decreases with s, because an increase in the bed upslope produces a decrease of both Re_b and Fr (Figures 6(a) and 6(b)). Figure 6(c) shows that, at fixed R, the entrainment decreases with an increase in θ. In addition, for a fixed θ, E_{bulk} is lower in the $R > 1$ cases than in the cases with $R \le 1$: if R decreases, Fr and Re_b increase and E_{bulk} increases as a consequence. Thus, a dependence of the entrainment parameter on both θ and R is observed. Finally, the partial-depth cases show smaller values of the entrainment parameter than the $\phi = 1$ cases.

The same values of E_{bulk} plotted in Figure 6 are reported in Figure 7 together with previous laboratory[2,3,38–40] and field[41–45] entrainment evaluations. Present entrainment parameters refer to density currents produced by the lock-exchange technique, i.e., unsteady density currents, while the experimental results shown in Figure 7 refer to density currents produced by a continuous source of salty water, i.e., steady density currents flowing downslope. Figure 7 shows that the entrainment parameter of the present study, i.e., unsteady density currents (with $1615 < Re_b < 10010$ and $0.24 < Fr < 0.74$), has the same order of magnitude ($E \sim 10^{-2}$) as that found for steady density currents with higher Fr ($1 < Fr < 6$) and lower Re_b ($40 < Re_b < 1386$). Thus, the dependence of E_{bulk} on both Re_b and Fr is confirmed, because the order of magnitude of the entrainment parameter of the present simulations is comparable to the entrainment of gravity currents generated by different experimental procedures and characterized by different values of Fr and Re_b. In addition, in agreement with previous studies,[2,3,9,17] Figure 7 shows the occurrence of mixing also for subcritical flows ($Fr^2 < 1.25$), not included in the entrainment parametrization of Turner.[46] Finally, the empirical entrainment relation adopted in Adduce, Sciortino, and Proietti,[9] two-layer
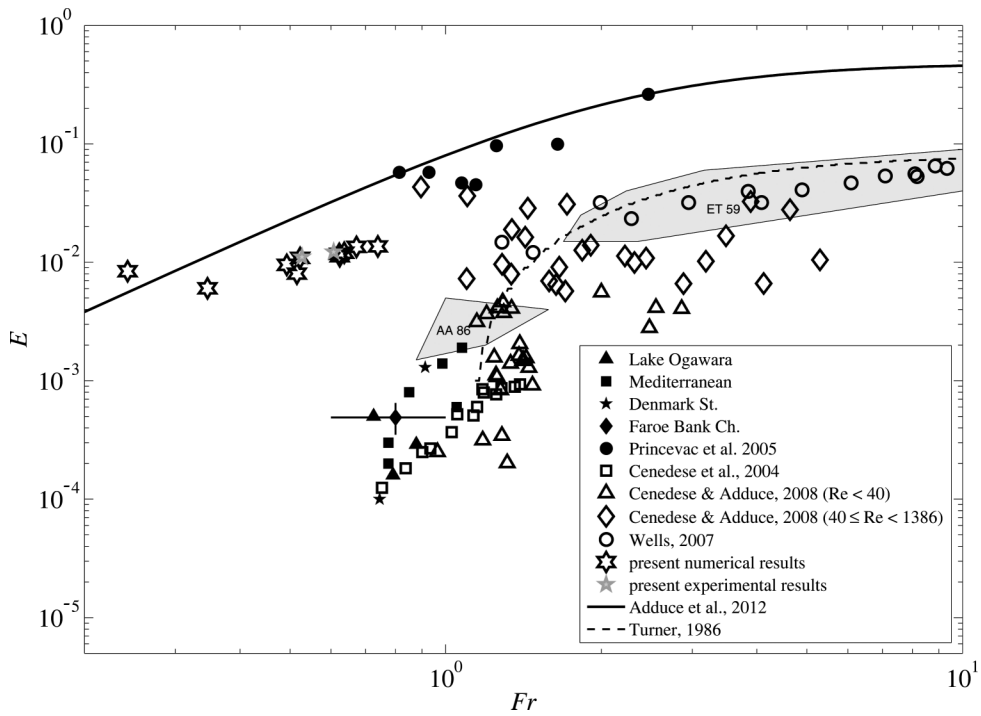
FIG. 7. Bulk entrainment parameter versus Fr: comparison of present numerical and experimental results with previous field data (solid symbols), laboratory measurements (open symbols), shaded areas for experiments by Ellison and Turner[39] and Alavian,[40] entrainment laws suggested by Turner[46] (dashed line), and Adduce, Sciortino, and Proietti[9] (solid line).

shallow water simulations of lock-release gravity currents, agrees with the present entrainment evaluations.

V. POTENTIAL ENERGY BUDGET AND IRREVERSIBLE MIXING

The potential energy budget is a useful method for the evaluation of irreversible mixing processes, as shown in Winters *et al.*,[27] and was successfully used to investigate the dynamics of lock-release gravity currents moving over horizontal boundaries.[47] This method of Winters *et al.*[27] is herein applied for the first time to analyse mixing in gravity currents propagating up a slope. In the present case, the potential energy E_p is defined as

$$E_P(t) = g \int_V \langle \rho(x,y,t) \rangle \, l \, dV, \tag{21}$$

where V is the entire volume of the fluid, l is the vertical distance from a horizontal plane of reference, and $\langle \rho \rangle$ is the spanwise averaged density field (Figures 8(a) and 8(c)). E_p can be affected by adiabatic processes (without exchanges of heat or mass) and by diabatic ones. The background potential energy E_b is here defined as

$$E_b(t) = g \int_V \langle \tilde{\rho}(x,y,t) \rangle \, l \, dV, \tag{22}$$

where $\langle \tilde{\rho} \rangle$ is the spanwise averaged density field, corresponding to the minimum state of the potential energy (Figures 8(b) and 8(d)). Thus, E_b can be evaluated from a spatial redistribution of the fluid particles in a stable horizontally stratified configuration, attained by means of adiabatic processes. Provided that spanwise gradients of ρ are not large compared with streamwise gradients, the quantities E_p and E_b calculated using $\langle \rho \rangle$ and $\langle \tilde{\rho} \rangle$ can be a useful approximation of E_p and E_b defined in Winters *et al.*[27,47,48] The available potential energy E_a is defined as the difference between
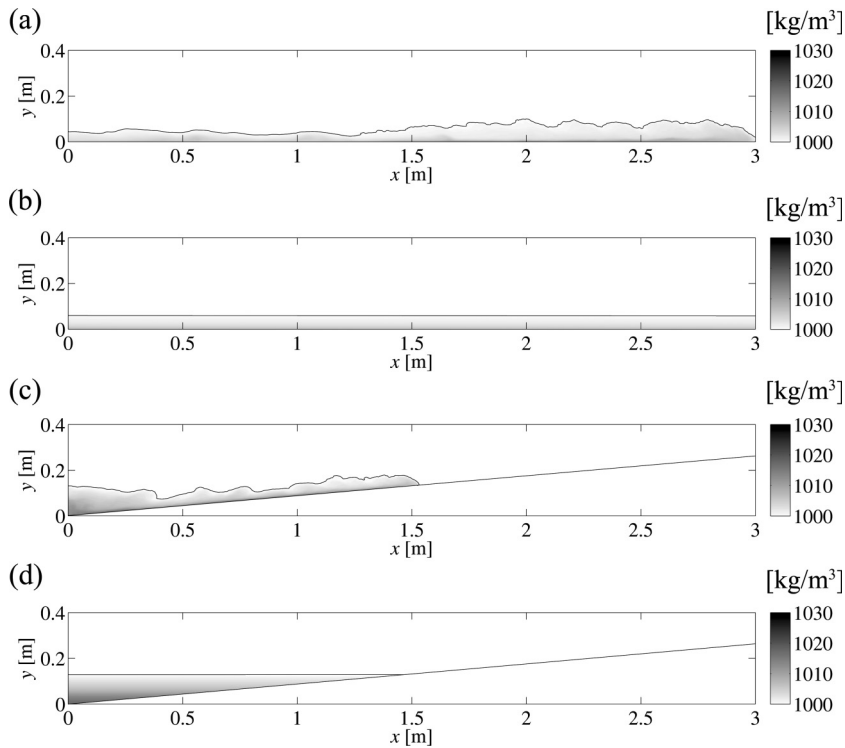
13

FIG. 8. Energy budget method. (a) Distribution of $\langle \rho \rangle$ in RUN0 ($\theta = 0°$, $R = 2$) for the evaluation of E_p at $T^* = 93.8$; (b) distribution of $\langle \tilde{\rho} \rangle$ in RUN0 for the evaluation of E_b at $T^* = 93.8$; (c) distribution of $\langle \rho \rangle$ in RUN3 ($\theta = 5°$, $R = 2$) for the evaluation of E_p at $T^* = 46.1$; (d) distribution of $\langle \tilde{\rho} \rangle$ in RUN3 for the evaluation of E_b at $T^* = 46.1$.

E_p and E_b,

$$E_a(t) = E_p(t) - E_b(t). \tag{23}$$

In Figure 8, two density distributions $\langle \rho \rangle$ and the corresponding $\langle \tilde{\rho} \rangle$ are shown for RUN0 and RUN3. Adiabatic processes can modify E_p through a redistribution of ρ in a different configuration, without altering the background energy. In this way, changes in the distribution of density are related to changes in E_a and E_b.[27] Specifically, conversion of potential energy into kinetic energy, caused by adiabatic reversible processes, can be analysed using the available potential energy E_a. On the other hand, variation in E_b can be used to highlight the occurrence of irreversible mixing.

The potential energy budget versus x_f^* is shown in Figure 9 for the different cases characterized by $R = 2$, with E_p, E_b, and E_a normalized so that the minimum of E_b at the initial time is zero, and the maximum of E_p at $t = 0$ is equal to 1. The potential energy budget for the other simulations (not displayed) shows a behaviour similar to the one observed in Figure 9. From Figure 9, it is apparent that the three contributions are affected by the bottom upslope. Figure 9(a) describes the evolution of the potential energies for a horizontal gravity current. During the slumping phase, E_p rapidly decreases as the front of the gravity current advances and E_b increases with x_f^*, indicating the occurrence of irreversible mixing processes. After the slumping phase, both E_p and E_b vary monotonically: E_p decreasing and E_b increasing almost linearly. As a result, E_a decreases monotonically with x_f^* (Figure 9(a)).

In RUN1, RUN2, and RUN3 ($R = 2$, $\theta \neq 0$), energy contributions are substantially different from the horizontal case. After the current forms in the first two lock-lengths, the potential energy increases with x_f^* (Figures 9(b)-9(d)), as the nose of the current climbs up the slope. Specifically, during the run with the steepest inclination of the bottom shown in Figure 9(d), E_b increases sharply for $x_f^* < 10$. From the beginning of the self-similar phase on, E_p ceases growing and begins to decrease. The curvature of the time evolution of E_b changes compared with the previous cases, eventually approaching a horizontal asymptote at the end of the simulation. During the slumping
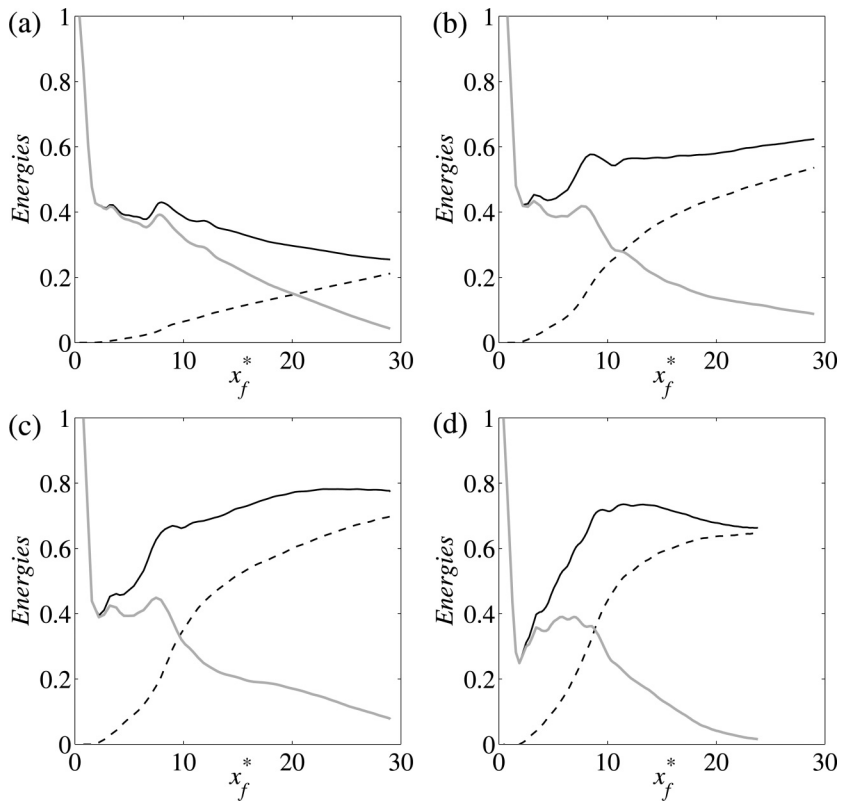
FIG. 9. Potential energy budget for the runs with $R = 2$. Potential energy (solid line), background potential energy (dashed line), and available potential energy (grey line) versus x_f^*. (a) RUN0 ($\theta = 0°$); (b) RUN1 ($\theta = 1.4°$); (c) RUN2 ($\theta = 2.5°$); and (d) RUN3 ($\theta = 5°$).

phase, the rate of increase of E_b in RUN3 is much larger than in the horizontal case due to the different equilibrium configuration of the spatial density distribution (Figures 8(b) and 8(d)). While a gravity current propagates up a slope, a reverse flow occurs, accumulating dense fluid at the left wall of the tank, and causing E_b to increase substantially: heavy fluid is present at higher vertical levels than in the horizontal case. At the same time, the reverse flow weakens the forward propagating gravity current reducing E_p in the self-similar phase. At the end of the simulation, the residual current stops flowing forward and the accumulated fluid stratifies in the minimal potential energy configuration, making E_p and E_b almost identical.

The curves of E_b versus x_f^* for all the $R = 2$ cases are shown in Figure 10(a). In the horizontal case, E_b increases in a quasi-linear way with x_f^*. Conversely, for the other cases, the curve of E_b approximates the logarithmic behaviour and, the steeper the bed upslope, the faster E_b approaches a horizontal asymptote. During the slumping phase, the slope of E_b is higher for the up-sloping cases, while it decreases with the inclination of the bottom during the self-similar phase. This is connected to the different equilibrium configurations of the horizontal and the upsloping cases (Figures 8(b) and 8(d)) and obviously does not indicate an increase of irreversible mixing related to the increase of the bed slope.

In order to make the different runs comparable among them in terms of irreversible mixing, the quantity E_{bH} is calculated by redistributing the fluid particles at the minimum of E_p in a tank with a horizontal bed. In this way, only the changes in the pdf of ρ are highlighted. In Figure 10(b), E_{bH} is plotted and is calculated distributing the density particles at the minimum of E_p on a horizontal bottom for all the $R = 2$ cases. In this way, the accumulation area does not affect E_{bH} and the different runs can be compared. During the slumping phase, small differences are detected between the different configurations. In the following times ($x_f^* > 8$), the curves of the different upslopes diverge. Changes in E_{bH} are always visible during all of the simulations, indicating the presence of
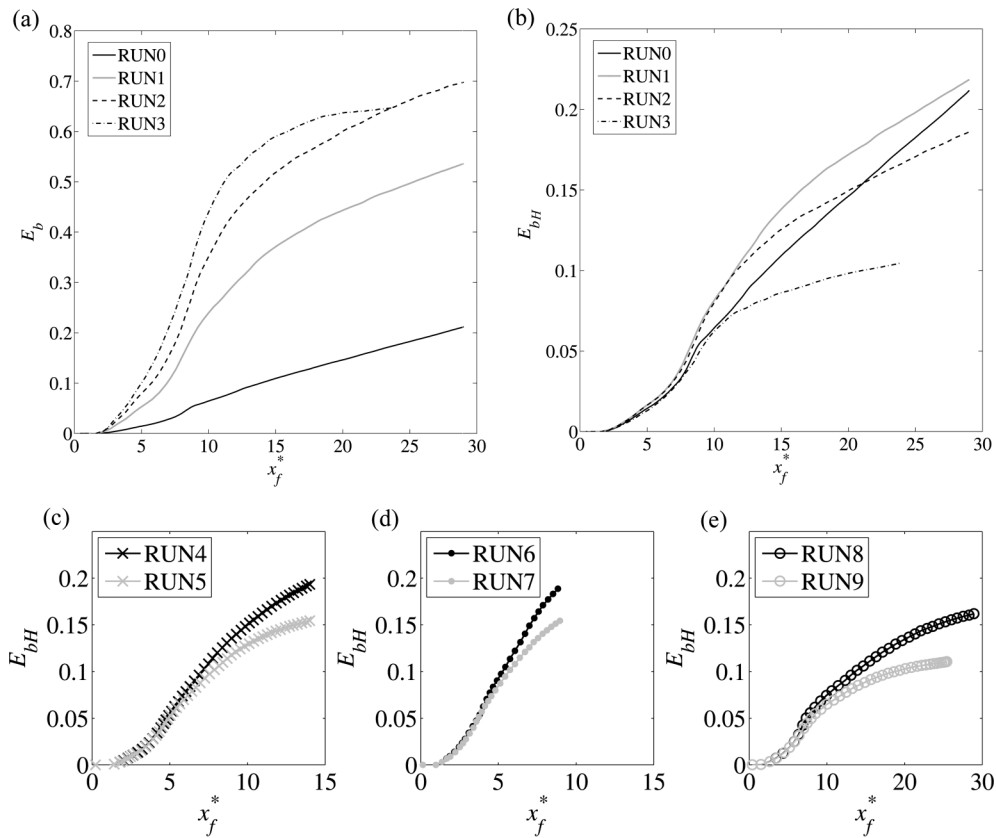
FIG. 10. Background potential energy versus x_f^*. (a) E_b calculated with the real inclined bottom for the cases with $R = 2$; (b) E_{bH} calculated with an equivalent horizontal bottom for the cases with $R = 2$; (c) E_{bH} for the cases with $R = 1$; (d) E_{bH} for the cases with $R = 0.67$; and (e) E_{bH} for the cases with $R = 1$ and $\phi = 0.5$.

mixing both in the slumping and in the self-similar phases. The inclination of the curve of E_{bH} is higher for RUN1 than for RUN3, showing that, as expected, the irreversible mixing is more efficient when the bed upslope is small. Figures 10(c)-10(e) show E_{bH} versus x_f^* in the other simulations, namely, the $R = 1$, $R = 0.67$, and the $\phi = 0.5$ cases, respectively. A lower inclination of E_{bH} as θ increases is visible in all of the cases tested. Thus, in all of the initial configurations considered, a faster variation of E_{bH} is visible for low values of θ than in the cases with high values of θ, indicating the occurrence of more pronounced irreversible mixing processes when the upslope is small. The influence of R on mixing is detectable by comparing, for fixed values of θ, the slopes of the curves of E_{bH} in Figures 10(b)–10(d): mixing increases as R decreases. Finally, Figures 10(c) and 10(e) show the effect of ϕ on mixing: a lower irreversible mixing occurs in the partial-depth cases than in the full-depth ones.

VI. CONCLUSIONS

Entrainment and mixing in gravity currents propagating up a sloping bottom were investigated in this paper through large eddy simulations. Three parameters, namely, the angle between the bottom boundary and the horizontal direction θ, the aspect ratio of the initial volume of the dense fluid in the lock R, and the depth ratio ϕ, were considered and the effect of their variation on both the dynamics of the current and mixing was discussed. Laboratory experiments were also realized in order to assess the reliability of the implementation of the numerical model and a good agreement between the numerical results and the laboratory measurements was found, for both the front propagation and the bulk entrainment parameter.

The classical features of a gravity current were observed in all of the cases herein simulated, with the transition through the different flow regimes known in the literature for horizontally propagating gravity currents. Overall, a first conclusion of this study is that the dynamics of a lock-release gravity current are affected by the presence of an upslope, which causes a reduction in the current front velocity and the occurrence of an accumulation region of dense stratified fluid in the initial part of the tank. For fixed values of R and ϕ, a decrease in the front velocity with the increase in the steepness of the bottom was observed. For the upsloping cases, a thinner profile of the dense current and smoother interface between the dense and the ambient fluids were detected when compared with the horizontal case.

Entrainment and mixing were investigated by using two different approaches: two entrainment parameters were defined (E_{local} and E_{bulk}) and the energy budget method of Winters et al.[27] was applied. The entrainment parameters were found to depend on both Fr and Re and as the bottom upslope increased, a decrease in the entrained ambient fluid was observed. At the end of all the simulations, E_{bulk} reached values of the order of 10^{-2}, in agreement with previous studies. An increase in the aspect ratio of the lock was associated with a decrease in the entrainment parameter; partial-depth gravity currents revealed the occurrence of less vigorous entrainment processes. In addition, the present entrainment evaluations of subcritical lock-release gravity currents, characterized by high Re, had an order of magnitude of 10^{-2}, which was in agreement with previous findings on the entrainment of steady supercritical gravity currents down a slope, characterized by a lower Re. Finally, the potential energy of the flow was analysed, through the application of the energy budget method of Winters et al.[27] in order to detect irreversible mixing processes occurring during the development of the current. The application of this method confirmed that all of the parameters varied in the present study (R, θ, and ϕ) affect mixing, in agreement with the findings on entrainment. Irreversible mixing processes were observed during the entire time evolution of the gravity current for all cases investigated. During the slumping phase, the effect of the bottom upslope on mixing was negligible. On the other hand, during the self-similar phase as the bottom upslope increased, less effective mixing occurred. Finally, mixing was found to decrease as R increases, and low mixing occurs in partial-depth gravity currents, i.e., $\phi < 1$, if compared with the full-depth ones, i.e., $\phi = 1$.

[1] J. E. Simpson, *Gravity Currents: In The Environment and The Laboratory* (Cambridge University Press, 1997).

[2] C. Cenedese, J. A. Whitehead, T. Ascarelli, and M. Ohiwa, "A dense current flowing down a sloping bottom in a rotating fluid," J. Phys. Oceanogr. **34**, 188 (2004).

[3] C. Cenedese and C. Adduce, "Mixing in a density-driven current flowing down a slope in a rotating fluid," J. Fluid Mech. **604**, 369–388 (2008).

[4] J. Hacker, P. Linden, and S. Dalziel, "Mixing in lock–release gravity currents," Dynam. Atmos. Oceans **24**, 183–195 (1996).

[5] M. La Rocca, C. Adduce, G. Sciortino, A. B. Pinzon, and M. A. Boniforti, "A two-layer, shallow-water model for 3d gravity currents," J. Hydraul. Res. **50**, 208–217 (2012).

[6] M. La Rocca, P. Prestininzi, C. Adduce, G. Sciortino, and R. Hinkelmann, "Lattice Boltzmann simulation of 3D gravity currents around obstacles," Int. J. Offshore Polar Eng. **23**(03), 178–185 (2013).

[7] J. Rottman and J. Simpson, "Gravity currents produced by instantaneous releases of a heavy fluid in a rectangular channel," J. Fluid Mech. **135**, 95–110 (1983).

[8] V. K. Birman, B. A. Battandier, E. Meiburg, and P. F. Linden, "Lock-exchange flows in sloping channels," J. Fluid Mech. **577**, 53–77 (2007).

[9] C. Adduce, G. Sciortino, and S. Proietti, "Gravity currents produced by lock exchanges: Experiments and simulations with a two-layer shallow-water model with entrainment," J. Hydraul. Eng.–ASCE **138**, 111–121 (2012).

[10] A. Dai, C. Ozdemir, M. Cantero, and S. Balachandar, "Gravity currents from instantaneous sources down a slope," J. Hydraul. Eng. **138**, 237–246 (2012).

[11] A. Dai, "High-resolution simulations of downslope gravity currents in the acceleration phase," Phys. Fluids **27**, 076602 (2015).

[12] L. J. Marleau, M. R. Flynn, and B. R. Sutherland, "Gravity currents propagating up a slope," Phys. Fluids **26**, 046605 (2014).

[13] V. Lombardi, C. Adduce, G. Sciortino, and M. L. Rocca, "Gravity currents flowing upslope: Laboratory experiments and shallow water simulations," Phys. Fluids **27**, 016602 (2015).

[14] C. S. Jones, C. Cenedese, E. P. Chassignet, P. F. Linden, and B. R. Southerland, "Gravity current propagation up a valley," J. Fluid Mech. **762**, 417–434 (2015).

[15] C. Cenedese and C. Adduce, "A new parameterization for entrainment in overflows," J. Phys. Oceanogr. **40**, 1835–1850 (2010).

[16] H. Nogueira, C. Adduce, E. Alves, and M. Franca, "Image analysis technique applied to lock-exchange gravity currents," Meas. Sci. Technol. **24**, 047001 (2013).

[17] H. Nogueira, C. Adduce, E. Alves, and M. Franca, "Dynamics of the head of gravity currents," Environ. Fluid Mech. **14**, 519–540 (2014).

[18] A. N. Ross, S. Dalziel, and P. Linden, "Axisymmetric gravity currents on a cone," J. Fluid Mech. **565**, 227–254 (2006).

[19] C. Härtel, E. Meiburg, and F. Necker, "Analysis and direct numerical simulation of the flow at a gravity-current head. I. Flow topology and front speed for slip and no-slip boundaries," J. Fluid Mech. **418**, 189–212 (2000).

[20] F. Necker, C. Härtel, L. Kleiser, and E. Meiburg, "Mixing and dissipation in particle-driven gravity currents," J. Fluid Mech. **545**, 339–372 (2005).

[21] M. Cantero, S. Balachandar, M. García, and D. Bock, "Turbulent structures in planar gravity currents and their influence on the flow dynamics," J. Geophys. Res. **113**, C08018, doi:10.1029/2007JC004645 (2008).

[22] S. Ooi, G. Constantinescu, and L. Weber, "Numerical simulations of lock-exchange compositional gravity current," J. Fluid Mech. **635**, 361–388 (2009).

[23] M. Cantero, J. Lee, S. Balachandar, and M. Garcia, "On the front velocity of gravity currents," J. Fluid Mech. **586**, 1–39 (2007).

[24] T. Tokyay, G. Constantinescu, and E. Meiburg, "Lock-exchange gravity currents with a high volume of release propagating over a periodic array of obstacles," J. Fluid Mech. **672**, 570–605 (2011).

[25] M. M. Nasr-Azadani and E. Meiburg, "Turbidity currents interacting with three-dimensional seafloor topography," J. Fluid Mech. **745**, 409–443 (2014).

[26] A. S. Safrai and I. V. Tkachenko, "Numerical modeling of gravity currents in inclined channels," Fluid Dyn. **44**, 22–30 (2009).

[27] K. Winters, P. Lombard, J. Riley, and E. D'Asaro, "Available potential energy and mixing in density-stratified fluids," J. Fluid Mech. **289**, 115–128 (1995).

[28] V. Armenio and S. Sarkar, "An investigation of stably stratified turbulent channel flow using large-eddy simulation," J. Fluid Mech. **459**, 1–42 (2002).

[29] J. R. Taylor, S. Sarkar, and V. Armenio, "Large eddy simulation of stably stratified open channel flow," Phys. Fluids **17**, 116602 (2005).

[30] S. Salon, V. Armenio, and A. Crise, "A numerical investigation of the stokes boundary layer in the turbulent regime," J. Fluid Mech. **570**, 253–296 (2007).

[31] L. Ottolenghi, C. Adduce, R. Inghilesi, V. Armenio, and F. Roman, "Entrainment and mixing in unsteady gravity currents," J. Hydraul. Res. (in press).

[32] S. B. Pope, *Turbulent Flows* (Cambridge University Press, 2000), pp. 558–586.

[33] C. Meneveau, T. Lund, and W. Cabot, "A Lagrangian dynamic subgrid-scale model of turbulence," J. Fluid Mech. **319**, 353–385 (1996).

[34] Y. Zang, R. Street, and J. Koseff, "A non-staggered grid, fractional step method for time-dependent incompressible Navier-Stokes equations in curvilinear coordinates," J. Comput. Phys. **114**, 18–33 (1994).

[35] X. Liu and Y. Jiang, "Direct numerical simulations of boundary condition effects on the propagation of density current in wall-bounded and open channels," Environ. Fluid Mech. **14**(2), 387–407 (2013).

[36] H. Nogueira, C. Adduce, E. Alves, and M. Franca, "Analysis of lock-exchange gravity currents over smooth and rough beds," J. Hydraul. Res. **51**, 417–431 (2013).

[37] J. Turner, *Buoyant Convection from Isolate Sources. Buoyancy Effects In Fluids* (Cambridge University Press, 1973), pp. 165–206.

[38] M. G. Wells, "Influence of coriolis forces on turbidity currents and their sediment patterns," Proc. Euromech. Colloq. **477**, 331–343 (2007).

[39] T. H. Ellison and J. S. Turner, "Turbulent entrainment in stratified flows," J. Fluid Mech. **6**, 423–448 (1959).

[40] V. Alavian, "Behavior of density currents on an incline," J. Hydraul. Eng.–ASCE **112**, 27–42 (1986).

[41] J. F. Price and M. O. Barringer, "Outflows and deep water production by marginal seas," Prog. Oceanogr. **33**, 161–200 (1994).

[42] C. J. Dallimore, J. Imberger, and T. Ishikawa, "Entrainment and turbulence in saline underflow in lake Ogawara," J. Hydraul. Eng.–ASCE **127**, 937–948 (2001).

[43] J. B. Girton and T. B. Sanford, "Descent and modification of the overflow plume in the Denmark strait," J. Phys. Oceanogr. **33**, 1351–1364 (2003).

[44] C. Mauritzen, J. Price, T. Sanford, and D. Torres, "Circulation and mixing in the Faroese channels," Oceanogr. Res **52**, 883–913 (2005).

[45] M. Princevac, H. Fernando, and C. D. Whiteman, "Turbulent entrainment into natural gravity-driven flows," J. Fluid Mech. **533**, 259–268 (2005).

[46] J. S. Turner, "Turbulent entrainment: The development of the entrainment assumption and its application to geophysical flows," J. Fluid Mech. **170**, 431–471 (1986).

[47] A. Fragoso, M. Patterson, and J. J. S. Wettlaufer, "Mixing in gravity currents," J. Fluid Mech. **734**, R2 (2013).

[48] M. Patterson, C. Caulfield, J. McElwaine, and S. Dalziel, "Time-dependent mixing in stratified Kelvin-Helmholtz billows: Experimental observations," Geophys. Res. Lett. **33**, doi:10.1029/2006GL026949 (2006).